scientific reports

OPEN

On a high photocatalytic activity of high-noble alloys Au–Ag/TiO$_2$ catalysts during oxygen evolution reaction of water oxidation

Anum Shahid Malik[1,2], Taifeng Liu[3✉], Meena Rittiruam[1,2,4], Tinnakorn Saelee[1,2,5], Juarez L. F. Da Silva[6], Supareak Praserthdam[1,2✉] & Piyasan Praserthdam[2]

The analysis via density functional theory was employed to understand high photocatalytic activity found on the Au–Ag high-noble alloys catalysts supported on rutile TiO$_2$ during the oxygen evolution of water oxidation reaction (OER). It was indicated that the most thermodynamically stable location of the Au–Ag bimetal-support interface is the bridging row oxygen vacancy site. On the active region of the Au–Ag catalyst, the Au site is the most active for OER catalyzing the reaction with an overpotential of 0.60 V. Whereas the photocatalytic activity of other active sites follows the trend of Au > Ag > Ti. This finding evident from the projected density of states revealed the formation of the trap state that reduces the band gap of the catalyst promoting activity. In addition, the Bader charge analysis revealed the electron relocation from Ag to Au to be the reason behind the activity of the bimetallic that exceeds its monometallic counterparts.

In the current era, solar energy is confined for practical reasons and has increased the attention of both academia and industrial sectors. The essential worldwide goal of solar energy is to create electricity, and it is prospective to generate fuels from the waste of CO$_2$ and H$_2$O by induction of solar photochemistry. In the past 40 years, heterogeneous photocatalysis and photochemistry fields have developed comprehensively in return to demanding energy and environmental issues[1–8]. One of the most capable solutions for the energy problem is photocatalytic overall water oxidation (POWS), i.e., oxygen and hydrogen evolution[9,10]. Water electrolysis—one of the most practical routes to produce hydrogen to establish clean and renewable energy cycles, accounted for up to 4% of the global hydrogen production[11,12]. Water electrolysis entails two half-cell reactions: the cathodic hydrogen evolution (HER) and anodic oxygen evolution (OER) reactions.

The metal/semiconductor photocatalysts have vast POWS potential and have drawn broad attention for a long time[13]. Since 1972, a typical semiconductor TiO$_2$ exhibited a suitable band structure for POWS as a photocatalyst[14]. Moreover, the TiO$_2$-supported Pt catalysts are competent of POWS under the range of ultraviolet light[15]. Evidently, the visible light POWS shows a higher potential for practical applications. However, due to the large bandgap of TiO$_2$, TiO$_2$-based photocatalysts POWS driven by visible light remains a great challenge[16–18]. Even though the bandgap of TiO$_2$ could be effectively narrowed down by elemental doping to harvest visible light, the energy levels introduced by impurity dopants can act as recombination centers for electrons and holes, resulting in a poor photocatalytic activity[19,20].

Moreover, it has been reported that various metals, e.g., Pt, Au, Ag, Pd, Ru, Cu, etc., loaded on semiconductors materials, e.g., TiO$_2$, RuO$_2$, etc. to confine photoexcited electrons through the formed Schottky junction can result in reserved charge recombination for photocatalytic enhancement[21–23]. When the material is operated in a visible light range, Au, Ag, and Cu can act as metallic plasmons and trigger localized surface plasmon resonance (LSPR)[24,25]. This energizes the electrons above the Fermi level from the occupied energy levels[26,27]. These electrons with high energy pass through the Schottky barrier of metal–semiconductor can be located in the semiconductor

^{1}High-Performance Computing Unit (CECC-HCU), Center of Excellence on Catalysis and Catalytic Reaction Engineering (CECC), Chulalongkorn University, Bangkok 10330, Thailand. ^{2}Center of Excellence on Catalysis and Catalytic Reaction Engineering (CECC), Chulalongkorn University, Bangkok 10330, Thailand. ^{3}National & Local Joint Engineering Research Center for Applied Technology of Hybrid Nanomaterials, Henan University, Kaifeng 475004, China. ^{4}Rittiruam Research Group, Bangkok 10330, Thailand. ^{5}Saelee Research Group, Bangkok 10330, Thailand. ^{6}São Carlos Institute of Chemistry, University of São Paulo, PO Box 780, São Carlos, SP 13560-970, Brazil. ✉email: tfliu@vip.henu.edu.cn; supareak.p@chula.ac.th
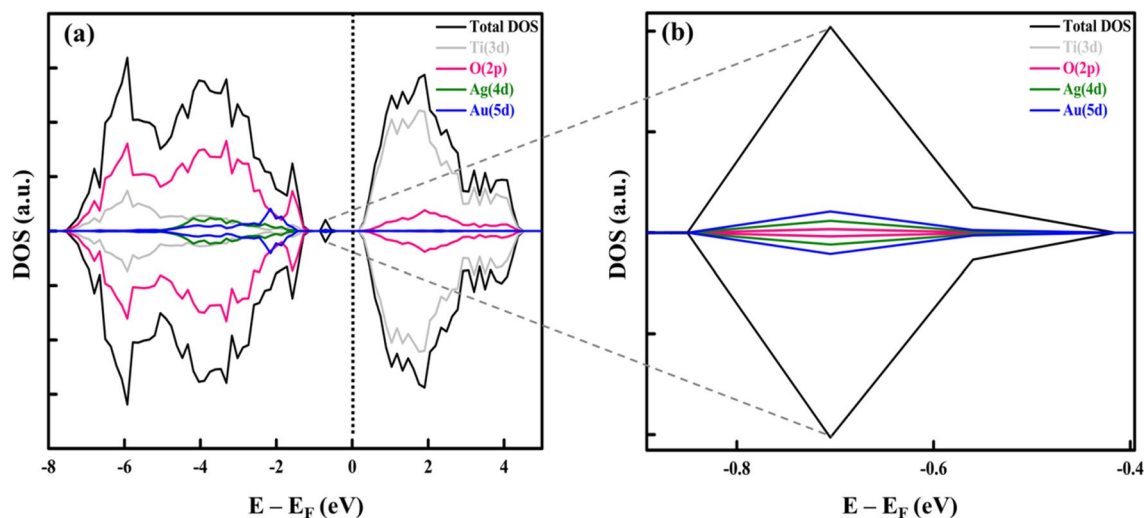
Figure 1. The density of states (DOS) profiles of (**a**) Au$_2$–Ag$_2$/TiO$_2$ (four atoms) cluster on bridging row oxygen vacant site and (**b**) the enlarged view of trap states which is majorly composed of Au(5d) and Ag(4d). (The DOS profile reflects the activity of the catalyst based on the analysis of bonding and antibonding states located at the left side of the E$_F$ and right side of the E$_F$ regions, respectively, where they are separated by the Fermi level designated at E$_F$ = 0 eV.

conduction band (CB), contributing to the competent charge separation and the photocatalytic reduction in the visible light region[28,29]. In the meantime, the positive charges left behind in the separated energy bands of plasmonic metals can be used to drive various oxidation reactions[30].

Therefore, metal-loaded TiO$_2$ (M/TiO$_2$, M = Au, Ag, Cu, etc.) plasmonic photocatalysts can be good candidates for the POWS that work under visible light. The Au, Ag, Cu plasmonic metals act as electron donors and generate electrons into TiO$_2$ under visible light. The differences in electron transfer from TiO$_2$ to the metal or metal to TiO$_2$ could drive different routes of water redox reaction resulting in various products distribution[31–33]. Silver (Ag) has been regarded as a promising candidate over gold (Au) due to its high catalytic activity. Water oxidation is a sluggish reaction in nature and artificial photosynthetic systems. Nevertheless, the plasmon resonance frequency of Ag is in the near-ultraviolet region, limiting its photocatalysis applications in the visible light region[34]. Consequently, the application of Ag-based photocatalysts remains challenging[35].

A substitute method to stabilize the Ag-based photocatalyst is to alloy the Ag metal with stable metals such as Au. These alloys comprising high content of noble metals are regarded as the high-noble alloys. In dentistry, such materials exhibit increased resistance to the corrosive environment–high stability[36]. When Ag is alloyed with Au, the stability is still maintained. The alloy could produce optical regulation due to their different plasmon response range and produce a prospect to tune the electronic structure, affecting Schottky barrier height and the plasmon-induced charges potentials[37]. In heterogeneous catalysis, although bimetallic alloys have been investigated extensively[38–40], the reliance of photocatalytic oxygen evolution reactions (OER) on the alloy components for water oxidation reaction is yet to be studied. The DFT calculations can be coupled with the experimental techniques to understand the enhanced activity of heterogeneous catalysts, e.g., Pd–Cu alloy nanoparticles supported on carbon support[41] and M$_4$/CeO$_2$ (ZrO$_2$) where M$_4$ is Pt, Pd, and Rh[42]. In addition, there are other theoretical and experimental works that have been carried out on similar interfaces. For instance, TiO$_2$-nanocluster adsorption on Ag and Au noble metal surfaces compared with that on graphene surfaces was recently investigated using density functional theory calculation[43]. This demonstrated that the electronic properties of the cluster on Ag and Au are not different, which helps to understand the experimental results[44]. The bimetallic nanocluster on a finite-size TiO$_2$ nano-wire was designed and presented as electronic properties, which are motivating to explore that in other bimetallic groups[45]. The importance of TiO$_2$ nanostructure and its energy application in terms of an experimental realization is summarized[46].

In this work, using DFT calculations and computational hydrogen electrode (CHE), we have evaluated the catalytic performance of Au–Ag/TiO$_2$ high noble alloys catalysts during water oxidation together with the investigation on roles of Au in such bimetallic cluster via the Au–Ag bimetallic cluster supported on rutile TiO$_2$ (110) models.

Results and discussion

Electronic properties of the catalysts: density of states analyses. We employed the HSE06 hybrid functional in DFT calculations for studying the band structure of the most stable structure, i.e., Au$_2$–Ag$_2$/TiO$_2$ embedded in place of oxygen vacancy. We used the Au$_2$–Ag$_2$ tetrahedral cluster supported on the rutile (110) surface due to its high stability[47]. The density of states (DOS) profiles for Au$_2$–Ag$_2$/TiO$_2$ are shown in Fig. 1. The valence band comprises O (2p), while the conduction band is majorly contributed by Ti (3d). In the forbidden gap, there are hybrid gap states found composed of Au (5d) and Ag (4d), with a significant contribution from
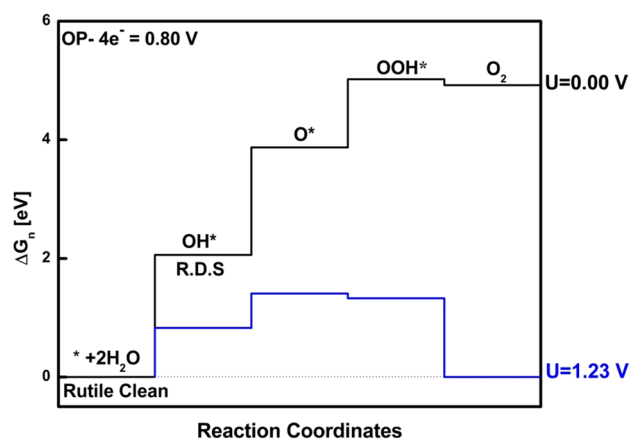
Figure 2. Free energy diagrams for OER through peroxo species on TiO_2 rutile (110) under external potential $U = 0.00$ V. (Black profile = O_2 evolution pathways go via the peroxo O^* intermediate. The rate-determining steps (R.D.S) are indicated with an arrow. The overpotential is displayed in the upper left corner. (recreated from[33]).

Au (5d). The Ag-5 s orbital is much higher in energy than the Au-6 s orbital energy, so a partial charge transfer from Au to Ag occurs[48].

Consequently, Au atoms tend to be negatively charged, while Ag atoms tend to be positively charged. The partial charge transfer from Au atoms to Ag atoms gives remarkable electrostatic stabilization, making the alloy formation more favorable than pure gold and silver clusters. Therefore, the equivalent mixing between Au and Ag atoms in the alloy formation will likely be more preferential. For Au_4/TiO_2 and Ag_4/TiO_2 tetrahedral structures positioned on bridging oxygen rows, vacancy results are shown in S.I (see fig S10 and S11).

It is well known that gold clusters have the lowest spin multiplicity as the ground state[49]. Previously, the spin effects of Au clusters on TiO_2 (110)[50] and other metal oxides[51] were studied. As a result, spin and electron distributions were assumed to have no effects in the case of noble metal atoms. Figure 1 shows that the spin-up and spin-down states of the DOS profiles of Ag 4d and Au 5d in Ag_4Au_4/TiO_2 are symmetrical, while in the case of Au_4/TiO_2, it exhibits slightly asymmetrical DOS shown in Figure S10 of the supplementary document.

TiO_2 surface can donate electrons and is ascribed to excess electrons from the defect state found inside the bandgap[34,52–54]. Ag and Au, relatively electronegative atoms, prefer to take the missing oxygen when creating an oxygen vacancy. Pulling an oxygen atom out of the bridging oxygen atom releases electron density, creating a vacancy site. This excess electron is transferred to Ag and Au atoms binding to the vacancy site. This implies that the support plays an active role in catalytic activity because it alters its chemical properties by transferring charge to Ag and Au[55]. In this work, DFT analyses are employed to understand the water oxidation mechanism on the interface between Au/Ag high noble alloys catalysts supported on rutile TiO_2 (110) and such a mechanism on the support itself. Thus, two main issues are focused, (1) determination of active regions on the surface (2) thermodynamically stable size and location of the active site cluster of initial (Au/TiO_2, Ag/TiO_2, $Au–Ag/TiO_2$) and cluster models (Au_4/TiO_2, Ag_4/TiO_2, $Au_2–Ag_2/TiO_2$).

Catalytic performance of TiO_2 support during oxygen evolution reaction (OER). We first discuss the water oxidation mechanism on clean rutile (110) TiO_2 surface. In Fig. 7d, we showed the pure surface of TiO_2 rutile (110), which is well investigated by many researchers theoretically and experimentally. The reported overpotential value for the pure surface is 0.80 eV with the rate-determining step OH^* as shown with recreation in Fig. 2 [33,56]. Furthermore, Malik et al. and Norskov et al. reported that on the clean or pure surface of TiO_2 mechanism of water oxidation proceeds through surface-bound peroxo O^* species. Thus, Ti was the only metal active site choice for studying water oxidation mechanisms.

Determination of active regions on the catalyst. Now we started analyzing with initial models of Au/TiO_2, Ag/TiO_2, and $Au–Ag/TiO_2$, where the model shown in Fig. 1a comprises one Ag atom replacing the bridging oxygen atom on the TiO_2 surface, while in Fig. 7b, one Au atom substituted an oxygen atom on the TiO_2 surface. When we studied $Au–Ag/TiO_2$ model (Fig. 7c), we tried different positioning of Au and Ag atoms, such as placing both atoms next to each other in the same bridging row or placing them on the same bridging row with the gap of one bridging oxygen atom in between Au and Ag (In S.I. see figure S1). The most stable position was when Au and Ag atoms were positioned on two bridging oxygen vacant sites in different rows, as shown in Fig. 7c. To study the OER mechanism on the $Au–Ag/TiO_2$ slab structure, the Ti atom was first chosen as an active site, and then the calculations were performed by choosing Au and Ag as an active site. For Au/TiO_2 and Ag/TiO_2 slab structures, the free energy diagrams are shown in S.I. in Figure S8 (a) and (b). The Ti active site was selected far from noble metal atoms. The OER data of the initial model for Fig. 7c, i.e., $Au–Ag/TiO_2$, is listed in Table 1. The OER data for Fig. 7a,b are shown in S.I. in table S2, and intermediates are shown in Figure S3 and S4.

From the OER results shown above in Fig. 3, it is indicated that the Au atom is preferably the active site with the lowest overpotential with an initial model. However, since Au and Ag atoms are placed on different bridging rows of oxygen vacancy sites, there is no interaction between noble metal atoms on the TiO_2 surface.

Active site	ΔG_{OH^*}	ΔG_{O^*}	ΔG_{OOH^*}	Overpotential (V)	Rate-determining steps
Au	1.54	3.88*	4.84	1.11	$O^* + H_2O \rightarrow HOO^* + \frac{1}{2}H_2$
Ag	0.68	3.29*	4.98	1.38	$O^* + H_2O \rightarrow HOO^* + \frac{1}{2}H_2$
Ti	0.03	0.17	3.58*	2.18	$HOO^* \rightarrow O_2 + \frac{1}{2}H_2$

Table 1. The relative free energies for each type of active site on the bimetallic Au–Ag/TiO$_2$ system shown in Fig. 7c, starting from the dissociation of a water molecule ($H_2O + ^* \leftrightarrow H^* + HO^*$) set as the reference point with zero energy. The propagating step is denoted as ΔG_{OH^*}, ΔG_{O^*}, and ΔG_{OOH^*} shown together with their overpotentials and rate-determining step. *The rate-determining steps.
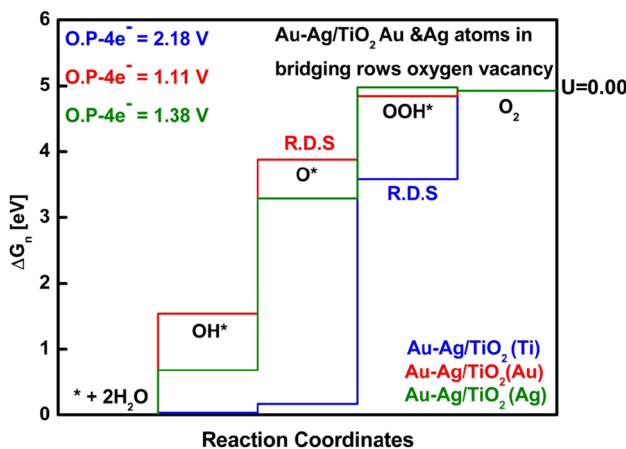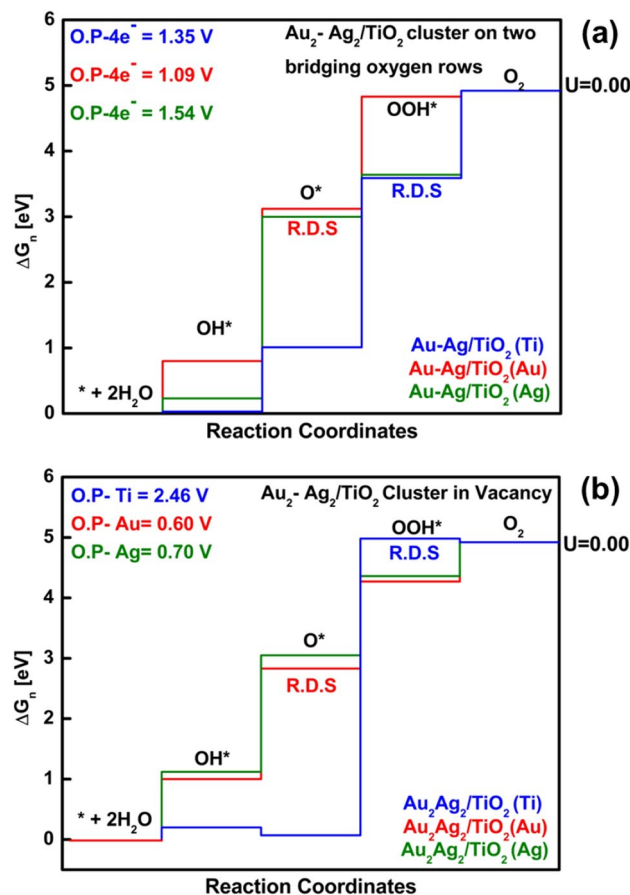

Figure 3. Comparative free energy diagram for Au–Ag/TiO$_2$ (Au and Ag placed in bridging vacant oxygen site) slab structure. Blue, red, and green profiles represent Ti, Au, and Ag as active sites. Overpotential for all energy profiles are shown in the upper left corner. The rate-determining step for Au and Au as active sites is O* while OOH* for Ti atom as an active site. R.D.S is rate-determining step.

OER performance of TiO$_2$ supported Au–Ag high-noble alloys catalysts.

An initial model is good enough to determine the active site; yet, Au and Ag atoms were placed on different bridging rows, so there was no interaction between Au and Ag atoms. Hence, no charge transfer could take place from Ag to Au. To understand the water oxidation mechanism at the interface of noble metal atoms cluster and TiO$_2$ metal oxide surface, we further extended calculations to use a 3-dimension tetrahedral cluster of (Au and Ag) atoms on the TiO$_2$ surface because of its stability. This structure we refer to as a cluster model. Our previous work[34] showed that the Au$_2$–Ag$_2$/TiO$_2$ structure is more suitable when embedded in the location of oxygen vacancy. Nevertheless, we show how the OER activity is affected when the tetrahedral cluster is placed on a stoichiometric surface at the two bridging oxygen rows (a different position), as shown in Fig. 8c. In the supplementary document, we have demonstrated OER intermediates of Au$_4$/TiO$_2$, Ag$_4$/TiO$_2$, and Au$_2$–Ag$_2$/TiO$_2$ when placed on two bridging rows (see figure S5 and S6). The comparative free energy diagram for Au$_4$/TiO$_2$, Ag$_4$/TiO$_2$ on two bridging rows is given in figure S9 (a) and (b) with the OER data (relative free energies) shown in table S3.

Figure 4a shows the results for Au$_2$–Ag$_2$/TiO$_2$ on two different bridging rows. The comparative free energy profile shows that the lowest overpotential is when Au was chosen as an active site. However, the OH*, O*, and OOH* steps were strongly bonded for the Ti active site than Au and Ag. Similar findings were observed for the model when Au$_2$–Ag$_2$/TiO$_2$ was placed on a bridging row oxygen vacancy. The O$_2$ evolution was preferred on the Au site, free energy diagram shown in Fig. 4b. From the above-shown results, it has been seen that either Au$_2$–Ag$_2$ cluster adsorb on TiO$_2$ surface by connecting to two bridging oxygen rows or an oxygen vacancy is created, and then the cluster is anchored into the vacant site; the perfect active site is Au. In all cases, Ti is the least preferred due to high overpotential. It was also found that the rate-determining step for OER on Au$_2$–Ag$_2$/TiO$_2$ surface is the O* intermediate, i.e., 2nd step when the active site is noble metal atoms, i.e., Au or Ag. While the rate-determining step for OER with Ti as an active site is OOH* intermediate, i.e., the 3rd step. For Au$_2$–Ag$_2$/TiO$_2$, the perfect active site is Au. When applied bias (U = 0 V), all steps go uphill thermodynamically.

When Au$_2$–Ag$_2$/TiO$_2$ cluster is adsorbed on two bridging rows, TiO$_2$ surface is stoichiometric; however, a remarkable change is noticed in overpotential when embedded on a vacant oxygen site. This change is attributed to the presence of oxygen vacancy because Au and Ag atoms are higher in electronegativity and prefer to stay in the place of oxygen vacancy. Therefore, there is excess electron density when the oxygen atom from the bridging row is removed. This "excess electron density" attaches the silver and gold clusters (with the ability of electronegativity) to the vacancy site. Moreover, when gold and silver atoms are bonded together in bimetallic clusters, there is a charge transfer from Ag to Au, which is accountable for making Au negatively charged and expected to be more active.

Figure 4. Comparative free energy diagrams for the evolution of O_2 on Au_2-Ag_2 cluster (**a**) placed on two bridging oxygen atoms, (**b**) embedded in the place of oxygen vacancy on bridging row[34]. The blue profile shows the energy for Ti active site, Green and red color shows energy profiles for Ag and Au active sites, respectively. The overpotential is shown in the upper left corner. *R.D.S* rate-determining step.

Active site	ΔG_{OH^*}	ΔG_{O^*}	ΔG_{OOH^*}	Overpotential (V)	Rate-determining steps
System: Au_2–Ag_2/TiO_2 with cluster on two bridging oxygen rows					
Au	0.80	3.12*	4.83	1.09	$O^* + H_2O \rightarrow HOO^* + \frac{1}{2}H_2$
Ag	0.23	3.00*	3.64	1.54	$O^* + H_2O \rightarrow HOO^* + \frac{1}{2}H_2$
Ti	0.03	1.01	3.59*	1.35	$HOO^* \rightarrow O_2 + \frac{1}{2}H_2$
System: Au_2–Ag_2/TiO_2 cluster on bridging row oxygen vacant site					
Au	1.00	2.83*	4.27	0.60	$O^* + H_2O \rightarrow HOO^* + \frac{1}{2}H_2$
Ag	1.12	3.05*	4.36	0.70	$O^* + H_2O \rightarrow HOO^* + \frac{1}{2}H_2$
Ti	0.20	0.07	3.76*	2.46	$HOO^* \rightarrow O_2 + \frac{1}{2}H_2$

Table 2. The relative free energies for each type of active sites on the Au_2–Ag_2/TiO_2 with a cluster on two bridging oxygen rows and bridging row oxygen vacant site shown in Figs. 8c and 9c, respectively, starting from the dissociation of a water molecule ($H_2O + ^* \leftrightarrow H^* + HO^*$) set as the reference point with zero energy. The propagating step is denoted as ΔG_{OH^*}, ΔG_{O^*}, and ΔG_{OOH^*} shown together with their overpotentials and rate-determining step. *The rate-determining steps.

For the cluster systems, the relative free energies of all the intermediates (OOH*, OH*, and O*) relative to the starting state (* + 2H₂O) are shown in Table 2. For all systems, we see that the trend in activity is the same for the active site, i.e., Au > Ag > Ti. For noble metal atoms, the rate-determining step is the O* step, and for transition metal, the rate-determining step is OOH*. Notably, the OOH* step is much less stable when the active site is Ti (blue curves in free energy diagrams) conversely the OH* and O* are more stable and vice versa for the noble metal active sites case (red and green curve for Au and Ag respectively in free energy diagrams).

Active site	ΔG_{OH^*}	ΔG_{O^*}	ΔG_{OOH^*}	Overpotential (V)	Rate-determining steps
System: Au$_4$/TiO$_2$, replacing bridging O atoms on the surface with Au$_4$ cluster in vacancy					
Au	0.15	1.92	3.73*	0.58 V	$O^* + H_2O \rightarrow HOO^* + \frac{1}{2}H_2$
Ti	0.63	2.93*	4.60	1.07 V	$HOO^* \rightarrow O_2 + \frac{1}{2}H_2$
System: Ag$_4$/TiO$_2$, replacing bridging O atoms on the surface with Ag$_4$ cluster in vacancy					
Ag	0.45	2.91*	3.72	1.23 V	$O^* + H_2O \rightarrow HOO^* + \frac{1}{2}H_2$
Ti	−0.13	0.67	3.55*	1.65 V	$HOO^* \rightarrow O_2 + \frac{1}{2}H_2$

Table 3. The relative free energies for each type of active sites on the monometallic Au$_4$/TiO$_2$ and Ag$_4$/TiO$_2$ cluster bridging row oxygen vacant site shown in Fig. 7a,b, starting from the dissociation of a water molecule ($H_2O + ^* \leftrightarrow H^* + HO^*$) set as the reference point with zero energy. The propagating step is denoted as ΔG_{OH^*}, ΔG_{O^*}, and ΔG_{OOH^*} shown together with their overpotentials and rate-determining step. *The rate-determining steps.
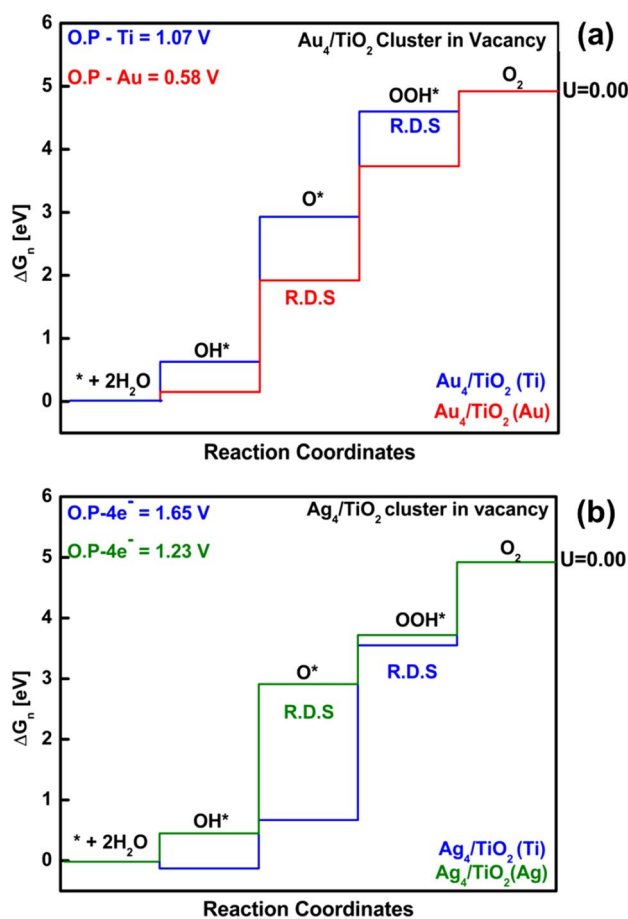
Figure 5. Comparative free energy diagram for (**a**) Ag$_4$/TiO$_2$ and (**b**) Au$_4$/TiO$_2$. Overpotential is shown in the upper left corner. The rate-determining step (R.D.S) for Ag and Au as active sites is O* while OOH* for Ti atom as an active site. Thus, the blue profile represents Ti as an active site, the red profile represents Au as an active site, and the green profile represents Ag as an active site.

OER performance of TiO$_2$ supported Ag and Au catalysts. As explained earlier, adsorption of Ag on TiO$_2$ surface becomes more stable when interacted with Au. Moreover, the photocatalytic property of Ag species is enhanced because Au promotes charge transfer from Ag to Au on the TiO$_2$ surface. To explain this phenomenon in-depth, we aimed to study the effect of only Au on TiO$_2$ and Ag on TiO$_2$ with cluster and initial model. We used the same strategy for choosing the active site and stable structure mentioned earlier for the bimetallic cluster. However, we only discuss the results of Au4/TiO$_2$ and Ag4/TiO$_2$ cluster models shown in Fig. 10a,b, and Table 3, respectively. Free energy diagrams are shown in Fig. 5a,b and for OER intermediates (see
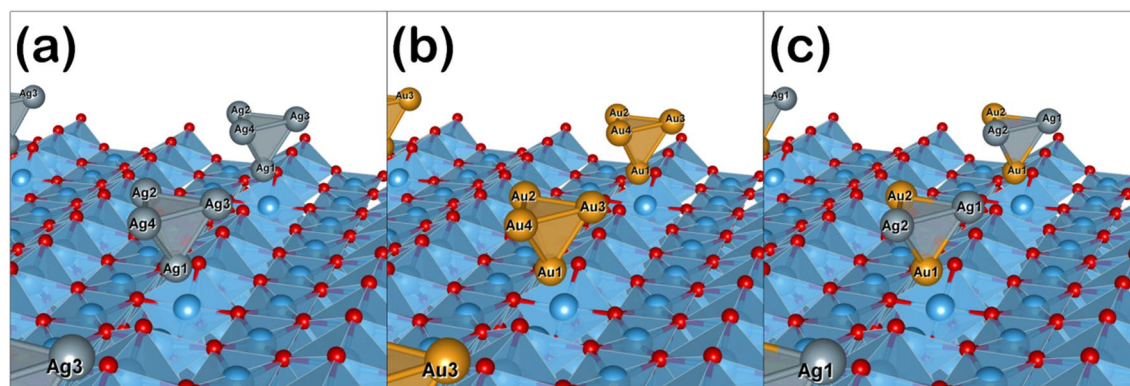
Figure 6. Configurations of the TiO$_2$-supported monometallic and bimetallic catalysts of (**a**) Ag$_4$/TiO$_2$, (**b**) Au$_4$/TiO$_2$, and (**c**) Au$_2$-Ag$_2$/TiO$_2$. The color code is blue for Ti, red for O, silver for Ag, and gold for Au.

S.I. figure S7). For Au$_4$/TiO$_2$ and Ag$_4$/TiO$_2$ clusters placed on two bridging rows, free energy diagrams are given in S.I figure S9.

Studying the OER mechanism on all Au and Ag clusters, i.e., Ag$_4$/TiO$_2$ and (b) Au$_4$/TiO$_2$, placed in bridging row oxygen vacancy, we found that overpotential for Ag active site was 0.53 V higher for Ag$_4$/TiO$_2$ when compared with Ag$_2$–Au$_2$/TiO$_2$, i.e., 0.70 V. However, for the Ti active site, overpotential is remarkably less, and a difference of 0.81 V was observed. If we compare Au$_4$/TiO$_2$ with Ag$_2$–Au$_2$/TiO$_2$ with Au active site, the overpotential remains the same almost. However, there are noticeable changes for the Ti active site, i.e., 1.39 V. So we conclude from our results that, in the case of any model, either initial or cluster, the active site is the preferably Au atom. In terms of overpotential, the trend of photocatalytic activity on all studied models is Au > Ag > Ti.

Insights into OER.   We mentioned earlier that Ag noble metal could be an excellent approach over Au for plasmonic photocatalytic activity; however, the plasmonic frequency of Ag is near the UV region responsible for limiting the catalytic activity of Ag-based photocatalyst. Therefore, we make a bimetallic alloy of Au and Ag. From our OER calculations, we have concluded that on Ag$_4$/TiO$_2$ over potential is higher for Ag active site, i.e., 1.23 V, for Au$_4$/TiO$_2$ overpotential is lower with Au active site, i.e., 0.58 V. But when Au and Ag are in a bimetallic cluster state, and we perform OER calculations on Au$_2$–Ag$_2$/TiO$_2$, the overpotential with Au and Ag active site is 0.60 V and 0.70 V, respectively. Hence, this proves that the presence of Au noble metal could stabilize the Ag and lead to better photocatalytic activity. Unfortunately, there are fewer reports of OER studies on noble metal-loaded TiO$_2$ structures. Wang et al.[57] reported the OER mechanism on Au/TiO$_2$ initial structure. Instead of removing Bridging oxygen, surface oxygen was removed and was further doped with Au atom. They only chose Ti as an active site. The rate-determining step was OOH* with an overpotential of 1.77 V. To provide further insight about noble metal-doped TiO$_2$ surface, the calculations were extended by using a small (four atoms) tetrahedral cluster for determining the OER activities. In the near future, studies with larger bimetallic clusters are needed to check if the trends observed here stay within the range of bimetallic particles.

Bader charge analysis.   Oxygen vacancy is one of the vital defects among all the defects known in TiO$_2$[58]. It has been discovered that oxygen vacancies can perform as significant adsorption and active sites for heterogeneous catalysis, which can sturdily sway the reactivity of metal oxides[59]. Theoretically, oxygen vacancies formation on TiO$_2$ is direct to the creation of unpaired electrons or Ti^{3+} centers, which possibly will form donor levels in the electronic structure of TiO$_2$[60]. Theoretical and experimental results indicate that the excess electrons are located on the oxygen vacancy states. When noble metal atoms (Au or Ag) are adsorbed on the TiO$_2$ surface, they tend to adsorb on the oxygen vacant site due to the high electronegativity of noble metal atoms.

We performed the Bader charge analysis to investigate the electron transfer between the metal active site (Au, Ag, or Ag–Au) and the catalyst surface for Ag$_4$/TiO$_2$, Au$_4$/TiO$_2$, and Ag$_2$–Au$_2$/TiO$_2$ system, as shown in Fig. 6. The calculated values are given in Table 4. The negative and positive signs refer to electron accumulation and depletion, respectively.

For the Ag$_4$/TiO$_2$ structure, the positive value of the Ag$_4$ cluster (+0.14 |e|) designates its role as an electron donor during its adsorption on the TiO$_2$ surface with an oxygen vacancy site. Moreover, a negative Bader charge of Ag1 (−0.23 |e|) together with the positive Bader charge of other surrounding Ag atoms (varies from +0.04 to +0.23 |e|) reveal electron transfer from the oxygen vacancy site to other Ag atoms: Ag2, Ag3, and Ag4, to Ag1 atom. Hence, the activity of the Ag1 atom is improved.

For Au$_4$/TiO$_2$ structure, the Au$_4$ cluster plays a role as an electron acceptor, taking electrons from the TiO$_2$ surface. Similar to the Ag$_4$/TiO$_2$ structure, the most negative Bader charge is found on the Au1 site, which specifies that the activity of the Au1 site is enhanced after its adsorption on the TiO$_2$ surface with oxygen vacancy site. In addition, the electron accumulations around the Au1 site is found to be two times higher than that of the Ag1. This suggested a high activity of the Au system.

For the Ag$_2$–Au$_2$/TiO$_2$ system, the whole bimetallic Ag$_2$–Au$_2$ cluster acted as an electron acceptor similar to the Ag cluster in the Ag$_4$/TiO$_2$ system. However, the total Bader charge value of the Ag$_2$–Au$_2$ cluster is less

System	Cluster	Bader charge (|e|)	
Ag$_4$/TiO$_2$	Ag$_4$	Ag$_4$ cluster	+0.14
		Ag1 atom	−0.23
		Ag2 atom	+0.10
		Ag3 atom	+0.04
		Ag4 atom	+0.23
Au$_4$/TiO$_2$	Au$_4$	Au$_4$ cluster	−0.32
		Ag1 atom	−0.41
		Ag2 atom	+0.01
		Ag3 atom	−0.05
		Ag4 atom	+0.13
Ag$_2$–Au$_2$/TiO$_2$	Ag$_2$–Au$_2$	Ag$_2$–Au$_2$ cluster	−0.14
		Au$_2$ subcluster	−0.69
		Ag$_2$ subcluster	+0.55
		Au1 atom	−0.48
		Au2 atom	−0.21
		Ag1 atom	+0.22
		Ag2 atom	+0.33

Table 4. Charge of each atom derived from the Bader charge analysis of Ag$_4$/TiO$_2$, Au$_4$/TiO$_2$ and Ag$_2$–Au$_2$/TiO$_2$ systems.
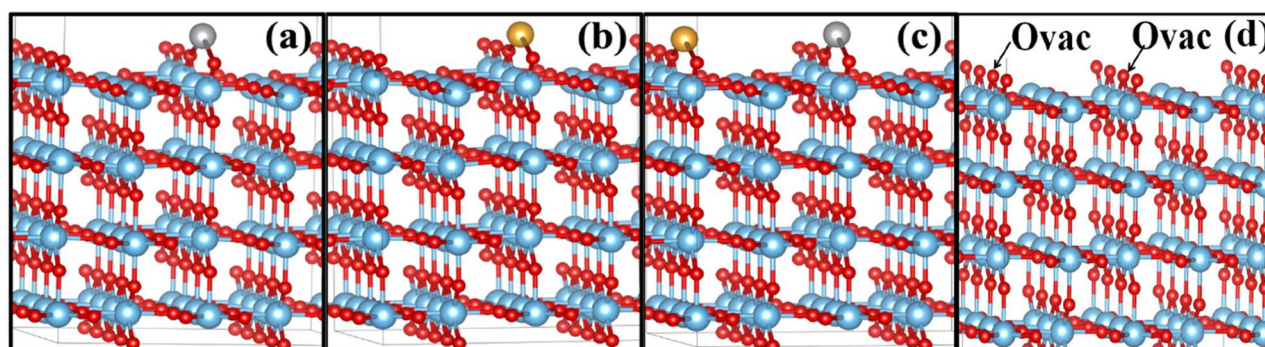
Figure 7. Initial model of one atom (**a**) Ag on TiO$_2$, (**b**) Au on TiO$_2$, (**c**) Au–Ag on TiO$_2$ (**d**) clean rutile TiO$_2$ (110) surface model.
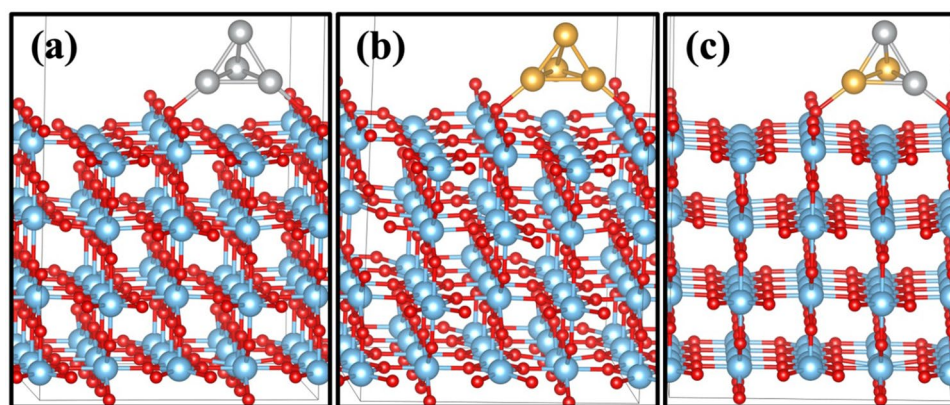
Figure 8. Four atoms cluster on two bridging rows of (**a**) Ag$_4$ on TiO$_2$, (**b**) Au$_4$ on TiO$_2$, and (**c**) Ag$_2$–Au$_2$ on rutile TiO$_2$ (110) surface model.

negative (-0.14 |e|). Considering the two-atom Ag (Ag_2) and two-atom Au (Au_2) cluster within the Ag_2–Au_2 cluster, it was found that the Au_2 subcluster holds a negative Bader charge of -0.69|e|, while the positive Bader charge was found in the Ag_2 subcluster of $+0.55$ |e|. This phenomenon describes the additional electron transfer from the Ag_2 to the Au_2 subcluster.

In addition, the activity of the Au1 active site in the Ag_2–Au_2 cluster is promoted via the electron transfer from the Ag site. Moreover, the Au1 site located at the vacancy site of the TiO_2 surface still has the most negative Bader charge value of -0.48 |e|. This Bader charge value of the Au1 atom in the Ag_2–Au_2 cluster is similar to the Au1 atom in the Au_4 cluster. Hence, the presence of Ag species in the Ag_2–Au_2 bimetallic cluster facilitates electron delocalization around Au1 and Au2, creating another active site—the Au2 site. Therefore, the activity of the bimetallic Ag_2–Au_2 cluster exceeds the monometallic cluster of Au4 and Ag4 clusters due to the presence of the Ag_2 subcluster, which donates additional electrons to the Au_2 subcluster.

Conclusion

In summary, we used density functional theory to investigate the role of Au metal in Au–Ag high noble alloys catalysts supported on TiO_2 on the performance during the oxygen evolution of water oxidation (OER), in which the catalysts are modeled as Au, Ag, and Au–Ag supported on rutile TiO_2 (110). Since doping of noble metal atoms increases the photocatalytic activity of TiO_2, the Ag noble metal is shown to have a promising catalytic activity among the groups. However, studying the reaction mechanism on such a surface is essential due to its low stability.

Combining Au (a more stable noble atom) into Ag-based TiO_2 forming bimetallic high-noble alloy catalysts can enhance photocatalytic activity. The study investigated the high-noble alloy cluster in terms of the most stable configuration verified by the most stable position of the metal-support interface, stability of the active site, optimal size, and the most active region of the catalyst for the OER during water oxidation. The most stable location of the metal-support interface for the Au–Ag high-noble alloy catalyst modeled by the Au_2–Ag_2/TiO_2 was found at the bridging row oxygen vacant site. On the performance of this high-noble alloy catalyst, the Au atom is always preferred as an active site for OER regardless of the size or position of the cluster. The photocatalytic activity trend indicated by an overpotential and active site preference is Au > Ag > Ti. Hence, in both cases of monometallic (Au and Ag) and bimetallic (Au–Ag), the Ti active site is least preferred.

With this positioning, the overpotential is much lower for the Au and Ag active site, i.e., 0.60 V and 0.70 V, indicating that the Au atom stabilizes Ag. Therefore, utilizing the high-noble alloy catalyst of Au–Ag can improve the oxygen evolution activity on the rutile TiO_2 (110) surface during the water oxidation reaction, promoting efficient hydrogen production and supporting the hydrogen economy.

In addition, the future design of high photocatalytic performance catalyst based on this study must consider the profiles from the Bader charge analysis, which suggested that the presence of the Ag atom can stabilize the Au atom via the electron transfer to the Au, where this generated the trap state between the valence band maximum (VBM) and the conduction band minimum (CBM) reducing the band gap of the catalyst promoting activity as supported by the projected density of states (DOS) profile of this Au–Ag/TiO_2 catalyst.

Methods

Computational details. *Density functional theory-based calculations.* We employed the first-principles spin-polarized density functional theory (DFT) calculations using the projector augmented wave (PAW) method applied in the Vienna Ab initio simulation package (VASP)[61,62]. For the exchange–correlation functional, the generalized gradient approximation (GGA)[63] of Perdew–Burke–Ernzerhof (PBE)[64] was used with the plane-wave cutoff energy of 400 eV. Ultra-soft pseudo-potential, the interaction between valence electrons and the ionic core[65], is used with $2s^2\ 2p^4$, $3d^2\ 4s^2$, $4d^{10}5s^1$, $5d^{10}6s^1$ as the valence electrons configuration for the O, Ti, Ag, and Au atoms, respectively. The Monkhorst and Pack scheme of k-point sampling was employed to integrate the first Brillouin zone[66], and a $3\times2\times1$ grid was used to obtain the geometry optimization and total energies for the rutile TiO_2 (110) surface. The applied residual forces for geometry optimization and convergence on the atoms were 0.01 eV/Å, and the self-consistent iteration awaits the tolerance for total energy to get to 10–4 eV. The optimized lattice parameters a = 11.83 Å, b = 12.99 Å, c = 30.08 Å, and $\alpha = \beta = \gamma = 90.00°$ for rutile (110). The calculations were done on a four-layered rutile TiO_2 (110) surface slab with a super-cell of $3\times2\times1$ where the bottom layer was fixed at bulk-truncated positions and the others were fully relaxed. Dipole correction was applied to all of the calculations. We calculated the energy position, valence band maximum (VBM), conduction band minimum (CBM), and trap states level for band structure calculations. For these properties, we carried out single-point energy calculations with the HSE06 functional[67] because they are known to provide a better description of the valence band (VB) and conduction band (CB), band edges, and band gaps (that are underestimated with PBE).

Catalyst model constructions. The OER mechanism was studied on the Au/TiO_2, Ag/TiO_2, and Au–Ag/TiO_2. For the initial model: We created an oxygen vacancy in the bridging row on the surface which was filled by gold atom in Au/TiO_2 model (Fig. 7a) and similarly Ag atom for Ag/TiO_2 (Fig. 7b); however, in the case of the Au–Ag/TiO_2 model, we replaced two bridging oxygen atoms from different bridging rows on the surface to replace Au and Ag atoms shown in Fig. 7c. Figure 7d shows the clean rutile (110) surface. We have demonstrated the bridging oxygen, which was pulled out to create oxygen vacancies. These configurations are shown to be at the most stable metal-support interface location. For the cluster model: We placed the tetrahedral cluster of 4 atoms Au_4, Ag_4, and Au_2–Ag_2 with different orientations on the surface, as shown in Figs. 8 and 9. We chose the cluster as a model because of its stability[68]. The result exhibited that the Au_2–Ag_2 alloy anchored on bridging
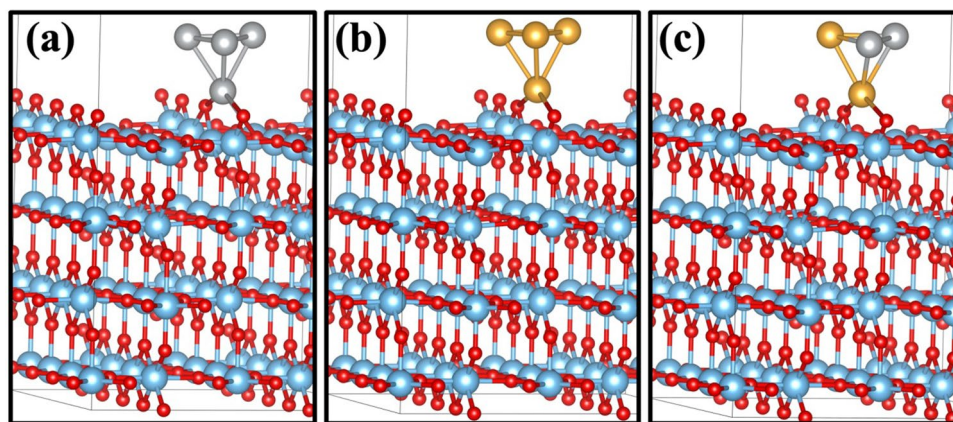
Figure 9. Four atoms cluster on bridging row oxygen vacant site of (**a**) Ag_4 on TiO_2, (**b**) Au_4 on TiO_2, and (**c**) Ag_2–Au_2 on rutile TiO_2 (110) surface model.
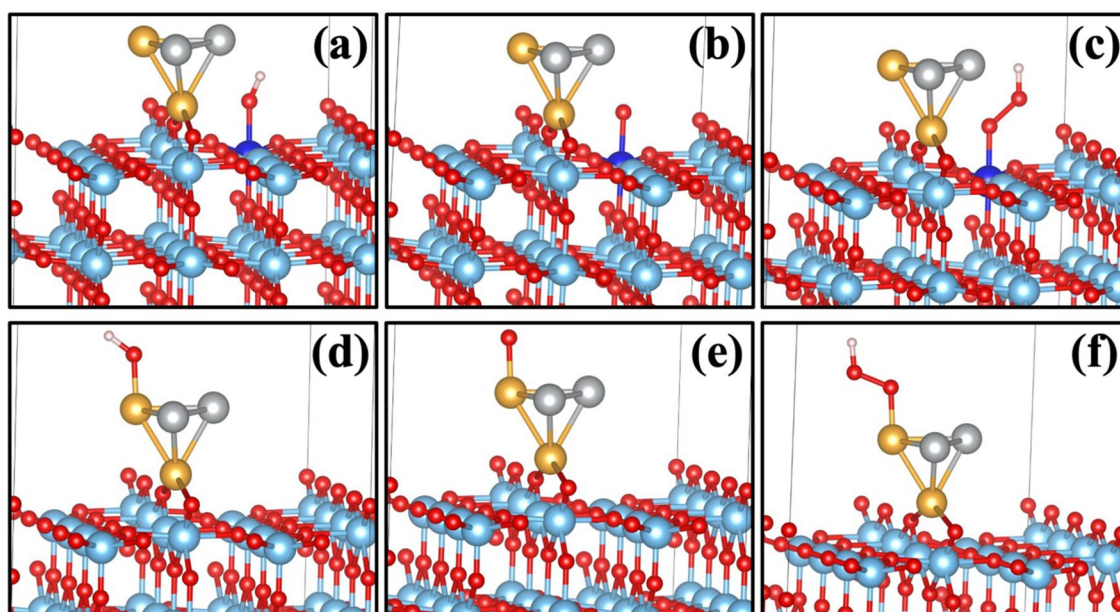
Figure 10. OER intermediates on Au_2–Ag_2/TiO_2 semiconductor surface with Ti active site marked blue in (**a**) OH*-Ti, (**b**) O*-Ti, (**c**) OOH*-Ti and with gold as active site shown in (**d**) OH*-Au, (**e**) O*-Au, and (**f**) OOH*-Au.

oxygen on top of the rutile TiO_2 (110) surface is the most stable, wherein Fig. 7d, a clean surface, is shown with the chosen oxygen vacancies marked as O_{vac}.

Evaluation of water oxidation performance. The reaction mechanism of water oxidation can occur with four proton-coupled electron transfer steps, where the initial step is the water adsorption process. Our calculations showed that water molecules tend to adsorb on the TiO_2 surface. We used the mechanism proposed by Rossmeisl et al.[69]. The OER mechanism is progressed in the following four steps as shown in equations 1–4, where ½ $H_2 \leftrightarrow H^+ + e^-$ is the half electrode reaction.

$$H_2O + * \rightarrow HO* + {}^1\!/_2\, H_2 \tag{1}$$

$$HO* \rightarrow O* + {}^1\!/_2 H_2 \tag{2}$$

$$O* + H_2O \rightarrow HOO* + {}^1\!/_2 H_2 \tag{3}$$

$$HOO* \rightarrow O_2 + {}^1\!/_2 H_2 \tag{4}$$

The OER intermediates are shown in Fig. 10a–f on Ti and Au as an active site, for Ag active site (see figure S2) in S.I. To evaluate the steps as mentioned above, it is expedient to characterize the free energies ΔG_{OH*}, ΔG_{O*} and ΔG_{OOH*} of the OH*, O*, OOH* intermediate states, and ΔG_{O_2} for the O_2 final stage, all determined relative to the resting state (* + $2H_2O$). In Sect. 1 of supplementary information (S.I), we have details of the determination of the free energies (including vibrational and entropy corrections). We can extract the reaction step-free energies from the relative free energies; ΔG_n (n = I, II, III, and IV) are written as equations 5–6.

$$\Delta G_I = \Delta G_{OH*} \tag{5}$$

$$\Delta G_{II} = \Delta G_{O*} - \Delta G_{OH*} \tag{6}$$

$$\Delta G_{III} = \Delta G_{OOH*} - \Delta G_{O*} \tag{7}$$

$$\Delta G_{IV} = \Delta G_{O2} - \Delta G_{OOH*} \tag{8}$$

The overpotential of reactions could be associated reliably to the proton and electron transfer to adsorbed species strongly bonded to the surface at the electrode potential. This reaction series starts with (* + $2H_2O$) on a metal active site leading to OH*, shown in steps I–IV. The diffusion of species and other surface reactions most likely depends weakly on the potential.

The theoretical overpotential is defined as:

$$\eta = \max [\Delta G_I, \Delta G_{II}, \Delta G_{III}, \Delta G_{IV}]/e - 1.23 \ [V] \tag{9}$$

Data availability
All data generated or analyzed during this study are included in this published article (and its Supplementary Information files).

References
1. Chen, X., Shen, S., Guo, L. & Mao, S. S. Semiconductor-based photocatalytic hydrogen generation. *Chem. Rev.* **110**, 6503–6570 (2010).
2. Fujishima, A., Rao, T. N. & Tryk, D. A. Titanium dioxide photocatalysis. *J. Photochem. Photobiol., C* **1**, 1–21 (2000).
3. Henderson, M. A. A surface science perspective on TiO2 photocatalysis. *Surf Sci Rep* **66**, 185–297 (2011).
4. Hoffmann, M. R., Martin, S. T., Choi, W. & Bahnemann, D. W. Environmental applications of semiconductor photocatalysis. *Chem. Rev.* **95**, 69–96 (1995).
5. Kamat, P. V. Meeting the clean energy demand: Nanostructure architectures for solar energy conversion. *J. Phys. Chem. C* **111**, 2834–2860 (2007).
6. Linsebigler, A. L., Lu, G. & Yates, J. T. Jr. Photocatalysis on TiO2 surfaces: Principles, mechanisms, and selected results. *Chem. Rev.* **95**, 735–758 (1995).
7. Matsuoka, M. *et al.* Photocatalysis for new energy production: Recent advances in photocatalytic water splitting reactions for hydrogen production. *Catal Today* **122**, 51–61 (2007).
8. Mills, A., Davies, R. H. & Worsley, D. Water purification by semiconductor photocatalysis. *Chem. Soc. Rev.* **22**, 417–425 (1993).
9. Ida, S. *et al.* A cocatalyst that stabilizes a hydride intermediate during photocatalytic hydrogen evolution over a rhodium-doped TiO2 nanosheet. *Angew. Chem.* **130**, 9211–9215 (2018).
10. Fu, Y. *et al.* Phase-modulated band alignment in CdS nanorod/SnSx nanosheet hierarchical heterojunctions toward efficient water splitting. *Adv. Funct. Mater.* **28**, 1706785 (2018).
11. Seh, Z. W. *et al.* Combining theory and experiment in electrocatalysis: Insights into materials design. *Science* **355** (2017).
12. Schalenbach, M., Zeradjanin, A. R., Kasian, O., Cherevko, S. & Mayrhofer, K. J. A perspective on low-temperature water electrolysis–challenges in alkaline and acidic technology. *Int. J. Electrochem. Sci* **13**, 1173–1226 (2018).
13. Lee, B.-H. *et al.* Reversible and cooperative photoactivation of single-atom Cu/TiO2 photocatalysts. *Nat. Mater.* **18**, 620–626 (2019).
14. Fujishima, A. & Honda, K. Electrochemical photolysis of water at a semiconductor electrode. *Nature* **238**, 37–38 (1972).
15. Cao, S. *et al.* Photocatalytic pure water splitting with high efficiency and value by Pt/porous brookite TiO2 nanoflutes. *Nano Energy* **67**, 104 (2020).
16. Wu, T. *et al.* Chlorine capped SnO2 quantum-dots modified TiO2 electron selective layer to enhance the performance of planar perovskite solar cells. *Sci. Bull.* **64**, 547–552 (2019).
17. Fang, S. & Hu, Y. H. Recent progress in photocatalysts for overall water splitting. *Int. J. Energy Res.* **43**, 1082–1098 (2019).
18. Mao, L., Huang, Y.-C., Fu, Y., Dong, C.-L. & Shen, S. Surface sulfurization activating hematite nanorods for efficient photoelectrochemical water splitting. *Sci. Bull.* **64**, 1262–1271 (2019).
19. Zhao, D. *et al.* Synergy of dopants and defects in graphitic carbon nitride with exceptionally modulated band structures for efficient photocatalytic oxygen evolution. *Adv. Mater.* **31**, 1903545 (2019).
20. Dozzi, M. V. & Selli, E. Doping TiO2 with p-block elements: Effects on photocatalytic activity. *J. Photochem. Photobiol. C* **14**, 13–28 (2013).
21. Li, J. *et al.* Solar hydrogen generation by a CdS-Au-TiO2 sandwich nanorod array enhanced with Au nanoparticle as electron relay and plasmonic photosensitizer. *J. Am. Chem. Soc.* **136**, 8438–8449 (2014).
22. Xiao, J. D., Han, L., Luo, J., Yu, S. H. & Jiang, H. L. Integration of plasmonic effects and schottky junctions into metal-organic framework composites: Steering charge flow for enhanced visible-light photocatalysis. *Angew. Chem. Int. Ed.* **57**, 1103–1107 (2018).
23. Xue, F. *et al.* Interfacial and dimensional effects of Pd co-catalyst for efficient photocatalytic hydrogen generation. *J. Phys. Chem. C* **122**, 25165–25173 (2018).
24. Zhang, P., Wang, T. & Gong, J. Solar Water Splitting: Mechanistic Understanding of the Plasmonic Enhancement for Solar Water Splitting (Adv. Mater. 36/2015). *Adv. Mater.* **27**, 5444–5444 (2015).

25. Lou, Z. *et al.* Plasmonic heterostructure TiO2-MCs/WO3− x-NWs with continuous photoelectron injection boosting hot electron for methane generation. *Adv. Funct. Mater.* **29**, 1808696 (2019).
26. Clavero, C. Plasmon-induced hot-electron generation at nanoparticle/metal-oxide interfaces for photovoltaic and photocatalytic devices. *Nat. Photon.* **8**, 95–103 (2014).
27. Brongersma, M. L., Halas, N. J. & Nordlander, P. Plasmon-induced hot carrier science and technology. *Nat. Nanotechnol.* **10**, 25–34 (2015).
28. Chen, J., Dong, C. L., Du, Y., Zhao, D. & Shen, S. Nanogap engineered plasmon-enhancement in photocatalytic solar hydrogen conversion. *Adv. Mater. Interfaces* **2**, 1500280 (2015).
29. Linic, S., Christopher, P. & Ingram, D. B. Plasmonic-metal nanostructures for efficient conversion of solar to chemical energy. *Nat. Mater.* **10**, 911–921 (2011).
30. Feng, B. *et al.* Achieving infrared detection by all-Si plasmonic hot-electron detectors with high detectivity. *ACS Nano* **13**, 8433–8441 (2019).
31. Zhang, Y., Hu, H., Huang, X. & Bi, Y. Photo-controlled bond changes on Pt/TiO 2 for promoting overall water splitting and restraining hydrogen–oxygen recombination. *J. Mater. Chem. A* **7**, 5938–5942 (2019).
32. Xue, F., Si, Y., Wang, M., Liu, M. & Guo, L. Toward efficient photocatalytic pure water splitting for simultaneous H2 and H2O2 production. *Nano Energy* **62**, 823–831 (2019).
33. Malik, A. S., Liu, T., Dupuis, M., Li, R. & Li, C. Water oxidation on TiO2: A comparative DFT study of 1e–, 2e–, and 4e—processes on rutile, anatase, and brookite. *J. Phys. Chem. C* **124**, 8094–8100. https://doi.org/10.1021/acs.jpcc.9b11450 (2020).
34. Haider, R. S. *et al.* Boosting photocatalytic water oxidation by surface plasmon resonance of AgxAu1-x alloy nanoparticles. *Nano Energy*, 106189 (2021).
35. Plodinec, M. *et al.* Black TiO2 nanotube arrays decorated with Ag nanoparticles for enhanced visible-light photocatalytic oxidation of salicylic acid. *J Alloy Compd* **776**, 883–896 (2019).
36. Wataha, J. C. Biocompatibility of dental casting alloys: A review. *J. Prosthet. Dent.* **83**, 223–234. https://doi.org/10.1016/S0022-3913(00)80016-5 (2000).
37. Strauss, I. *et al.* Characterization of multi-channel intraneural stimulation in transradial amputees. *Sci Rep UK* **9**, 1–11 (2019).
38. Link, S., Wang, Z. L. & El-Sayed, M. Alloy formation of gold–silver nanoparticles and the dependence of the plasmon absorption on their composition. *J. Phys. Chem. B* **103**, 3529–3533 (1999).
39. Papavassiliou, G. C. Surface plasmons in small Au-Ag alloy particles. *J. Phys. F Met. Phys.* **6**, L103 (1976).
40. Liu, J.-H., Wang, A.-Q., Chi, Y.-S., Lin, H.-P. & Mou, C.-Y. Synergistic effect in an Au– Ag alloy nanocatalyst: CO oxidation. *J. Phys. Chem. B* **109**, 40–43 (2005).
41. Goswami, C. *et al.* Boosting the electrocatalytic activity of Pd/C by Cu alloying: Insight on Pd/Cu composition and reaction pathway. *J. Colloid Interface Sci.* **587**, 446–456. https://doi.org/10.1016/j.jcis.2020.11.104 (2021).
42. Koga, H. *et al.* Effect of ceria and zirconia supports on NO reduction over platinum-group metal catalysts: A DFT study with comparative experiments. *Catal. Today* **332**, 236–244. https://doi.org/10.1016/j.cattod.2018.07.023 (2019).
43. Aguilera-Granja, F., Aguilera–del–Toro, R. H., Vogel, E. E. & Cisternas, E. TiO2 nano-clusters adsorbed on surfaces: A density-functional-theoretic study. *J. Phys. Chem. Solids* **150**, 109716. https://doi.org/10.1016/j.jpcs.2020.109716 (2021).
44. Biener, J., Farfan-Arribas, E., Biener, M., Friend, C. M. & Madix, R. J. Synthesis of TiO2 nanoparticles on the Au(111) surface. *J. Chem. Phys.* **123**, 094705. https://doi.org/10.1063/1.1999607 (2005).
45. Aguilera-Granja, F., Aguilera–del–Toro, R. H., Vogel, E. E. & Cisternas, E. Bimetalic (AuPt)4 nano-clusters adsorbed on TiO2 nano-wires: A density-functional-theoretic study. *J. Phys. Chem. Solids* **159**, 110275, https://doi.org/10.1016/j.jpcs.2021.110275 (2021).
46. Zhang, X.-F. *et al.* TiO2 nanorods loaded with AuPt alloy nanoparticles for the photocatalytic oxidation of benzyl alcohol. *J. Phys. Chem. Solids* **126**, 27–32. https://doi.org/10.1016/j.jpcs.2018.10.026 (2019).
47. Vijay, A., Mills, G. & Metiu, H. Adsorption of gold on stoichiometric and reduced rutile TiO2 (110) surfaces. *J. Chem. Phys.* **118**, 6536–6551. https://doi.org/10.1063/1.1557919 (2003).
48. Lee, H. M., Ge, M., Sahu, B. R., Tarakeshwar, P. & Kim, K. S. Geometrical and electronic structures of gold, silver, and gold–silver binary clusters: Origins of ductility of gold and gold–silver alloy formation. *J. Phys. Chem. B* **107**, 9994–10005. https://doi.org/10.1021/jp034826+ (2003).
49. Assadollahzadeh, B. & Schwerdtfeger, P. A systematic search for minimum structures of small gold clusters Aun (n=2–20) and their electronic properties. *J. Chem. Phys.* **131**, 064306. https://doi.org/10.1063/1.3204488 (2009).
50. Tada, K. *et al.* Effects of halogens on interactions between a reduced TiO2 (110) surface and noble metal atoms: A DFT study. *Appl. Surf. Sci.* **411**, 149–162. https://doi.org/10.1016/j.apsusc.2017.03.113 (2017).
51. Tada, K. *et al.* Effect of surface interactions on spin contamination errors of homogeneous spin dimers, chains, and films: model calculations of Au/MgO and Au/BaO systems. *Mol. Phys.* **119**, e1791989. https://doi.org/10.1080/00268976.2020.1791989 (2021).
52. Diebold, U. The surface science of titanium dioxide. *Surf. Sci. Rep.* **48**, 53–229. https://doi.org/10.1016/S0167-5729(02)00100-0 (2003).
53. Chrétien, S. & Metiu, H. Density functional study of the interaction between small Au clusters, Aun (n=1–7) and the rutile TiO2 surface. I. Adsorption on the stoichiometric surface. *J. Chem. Phys.* **127**, 084704. https://doi.org/10.1063/1.2770462 (2007).
54. Madsen, G. K. H. & Hammer, B. Effect of subsurface Ti-interstitials on the bonding of small gold clusters on rutile TiO2(110). *J. Chem. Phys.* **130**, 044704. https://doi.org/10.1063/1.3055419 (2009).
55. Vijay, A., Mills, G. & Metiu, H. *Adsorption of gold on stoichiometric and reduced rutile TiO2 (110) surfaces*. Vol. 118 (2003).
56. Valdés, Á., Qu, Z. W., Kroes, G. J., Rossmeisl, J. & Nørskov, J. K. Oxidation and photo-oxidation of water on TiO2 surface. *J. Phys. Chem. C* **112**, 9872–9879. https://doi.org/10.1021/jp711929d (2008).
57. Wang, S. *et al.* Positioning the water oxidation reaction sites in plasmonic photocatalysts. *J. Am. Chem. Soc.* **139**, 11771–11778. https://doi.org/10.1021/jacs.7b04470 (2017).
58. Pacchioni, G. Oxygen vacancy: the invisible agent on oxide surfaces. *ChemPhysChem* **4**, 1041–1047 (2003).
59. Polarz, S. *et al.* On the role of oxygen defects in the catalytic performance of zinc oxide. *Angew. Chem. Int. Ed.* **45**, 2965–2969 (2006).
60. Nowotny, M. K., Sheppard, L. R., Bak, T. & Nowotny, J. Defect chemistry of titanium dioxide. Application of defect engineering in processing of TiO2-based photocatalysts. *J. Phys. Chem. C* **112**, 5275–5300 (2008).
61. Kresse, G. & Furthmüller, J. Efficient iterative schemes for ab initio total-energy calculations using a plane-wave basis set. *Phys. Rev. B* **54**, 11169 (1996).
62. Kresse, G. & Joubert, D. From ultrasoft pseudopotentials to the projector augmented-wave method. *Phys. Rev. B* **59**, 1758 (1999).
63. Perdew, J. P. & Wang, Y. Accurate and simple analytic representation of the electron-gas correlation energy. *Phys. Rev. B* **45**, 13244 (1992).
64. Perdew, J. P., Burke, K. & Ernzerhof, M. Generalized gradient approximation made simple. *Phys. Rev. Lett.* **77**, 3865 (1996).
65. Vanderbilt, D. Soft self-consistent pseudopotentials in a generalized eigenvalue formalism. *Phys. Rev. B* **41**, 7892 (1990).
66. Monkhorst, H. J. & Pack, J. D. Special points for Brillouin-zone integrations. *Phys. Rev. B* **13**, 5188 (1976).
67. Heyd, J., Scuseria, G. E. & Ernzerhof, M. Hybrid functionals based on a screened Coulomb potential. *J. Chem. Phys.* **118**, 8207–8215. https://doi.org/10.1063/1.1564060 (2003).

68. Heiles, S., Logsdail, A. J., Schäfer, R. & Johnston, R. L. Dopant-induced 2D–3D transition in small Au-containing clusters: DFT-global optimisation of 8-atom Au–Ag nanoalloys. *Nanoscale* **4**, 1109–1115 (2012).

69. Rossmeisl, J., Qu, Z. W., Zhu, H., Kroes, G. J. & Nørskov, J. K. Electrolysis of water on oxide surfaces. *J. Electroanal. Chem.* **607**, 83–89. https://doi.org/10.1016/j.jelechem.2006.11.008 (2007).

Acknowledgements

Author contributions

S.P., A.M., M.R., and T.S. conceived the computational simulations. A.M. performed computational simulations. All authors performed data analyses, wrote, and reviewed the manuscript.

Competing interests

The authors declare no competing interests.

Additional information

Supplementary Information The online version contains supplementary material available at https://doi.org/10.1038/s41598-022-06608-7.

Correspondence and requests for materials should be addressed to T.L. or S.P.

Reprints and permissions information is available at www.nature.com/reprints.

Publisher's note Springer Nature remains neutral with regard to jurisdictional claims in published maps and institutional affiliations.